








Nonlocal bonding of a soliton and a blue-detuned state in a microcomb laser

Antonio Cutrona ^{1,2}, Vittorio Ceconi ^{1,2}, Pierre H. Hanzard^{2,3}, Maxwell Rowley², Debayan Das ^{1,2}, Andrew Cooper¹, Luke Peters^{1,2}, Luana Olivieri^{1,2}, Benjamin Wetzel ⁴, Roberto Morandotti⁵, Sai T. Chu ⁶, Brent E. Little⁷, David J. Moss⁸, Juan S. Toterogongora ^{1,2}, Marco Peccianti^{1,2} & Alessia Pasquazi ^{1,2}✉

Laser cavity-solitons can appear in a microresonator-filtered laser when judiciously balancing the slow nonlinearities of the system. Under certain conditions, such optical states can be made to self-emerge and recover spontaneously, and the understanding of their robustness is critical for practical applications. Here, we study the formation of a bonded state comprising a soliton and a blue-detuned continuous wave, whose coexistence is mediated by dispersion in the nonlinear refractive index. Our real-time dispersive Fourier transform measurements, supported by comprehensive theoretical analysis, reveal the presence of an elastic bonding between the two states, resulting in an enhancement of the soliton's robustness.

¹Emergent Photonics Research Centre, Dept. of Physics, Loughborough University, Loughborough LE11 3TU England, UK. ²Emergent Photonics Lab (Epic), Department of Physics and Astronomy, University of Sussex, Brighton BN1 9QH, UK. ³CORIA, UMR 6614, Université de Rouen Normandie, 76801 Saint Etienne du Rouvray, France. ⁴XLIM Research Institute, CNRS UMR 7252, Université de Limoges, Limoges 87060, France. ⁵INRS-EMT, 1650 Boulevard Lionel-Boulet, Varennes, Québec J3X 1S2, Canada. ⁶Department of Physics, City University of Hong Kong, Tat Chee Avenue, Hong Kong, China. ⁷QXP Technology Inc., Xi'an, China. ⁸Optical Sciences Centre, Swinburne University of Technology, Hawthorn, VIC 3122, Australia. ✉email: a.pasquazi@lboro.ac.uk

Nonlinear dissipative structures are striking formations occurring in dynamical systems that are far from equilibrium¹. Basic formations like dissipative solitons balance wave dispersion and nonlinear focusing together with gain and loss^{2,3}. These structures are ubiquitous in many fields, from chemistry⁴ and physics to biology⁵. Understanding their real-time, dynamic evolution is fundamental to advancing our knowledge of complex nonlinear and out-of-equilibrium systems, and is thus critical to developing next-generation optical sources.

While passive mode-locking remains the most established technology for pulsed lasers^{2,3}, recent advances have witnessed a myriad of different approaches for broadband optical generation. The discovery of temporal cavity-solitons in Kerr cavities has, in particular, provided an effective way of harnessing parametric gain, greatly advancing the field of microcombs or microresonator-based frequency combs^{6–23}. More recently, they have been observed in quantum cascade lasers^{21,24,25}. Based upon nonlinear wave-mixing that exists in most materials, parametric amplification can overcome the common bandwidth limitation of laser gain based on stimulated emission. These novel approaches have tremendously impacted many fields. In integrated optics, microcombs and quantum cascade lasers have formed the basis of breakthroughs in communications^{14,18,19}, metrology^{26–36} and quantum optics²⁰, while new fibre optic sources based on these concepts show enhanced functionalities^{37–41}. In this context, understanding the physical ingredients needed to create and sustain useful temporal structures beyond the established approaches of ultrafast gain saturation and filtering, typical of passive mode-locking, is particularly pressing and requires a holistic understanding of the system.

In this framework, we have recently shown that laser cavity-solitons in a microresonator-filtered fibre laser⁴² can self-emerge and recover thanks to the interaction of the slow nonlinearities of the system^{43,44}. Nonlocal nonlinearities such as thermal detuning^{45–48} and gain saturation⁴⁹ can have a significant impact on the global properties of such systems⁵⁰. They act on slower timescales than the fast ones (i.e., Kerr effect) and can be made to enhance the robustness of the solitary regimes. Slow nonlinearities played a role also in other configurations, such as lithium niobate microcombs⁵¹, Brillouin-mediated Kerr cavity-solitons^{52,53}, and dark solitons^{54,55}. Solitons sustained by such global effects can be exceptionally robust. Nonlocal nonlinearities, for instance, strongly underpinned the optical spatial solitons literature, famously preventing the catastrophic collapse of bidimensional solitons and allowing their observation and practical use^{56,57}.

The investigation of such pulses dynamics is significantly important. New measurement techniques for ultrafast optical pulse characterisation provide novel and exciting methods of understanding the formation and interaction between dissipative laser structures, from rogue waves to soliton molecules. In its beauty and simplicity, the Dispersive Fourier Transform (DFT) can measure the spectral transformation of a laser output in real-time and isolate its dynamics over different timescales^{58–70}. When connected with comprehensive modelling of the underlying physics, this technique can reveal the elementary interactions between different physical effects^{58–64}.

Among the different states that we have observed in our system, we will focus on states where solitons bond with independent continuous waves (CWs) thanks to an energy-dependent nonlinearity that underpins the interaction between them. In our system, solitons are generally found red-detuned with respect to the microcavity resonances⁴³. In such cases, however, the soliton state coexists with an independent, blue-detuned CW state in well-defined regions of the erbium-based laser emission spectrum. Interestingly, these states have also

been observed in configurations using a fibre-based Fabry-Perot resonator⁷¹ to filter the erbium laser cavity. Indeed, the coexistence of nonlinear states having different natures, such as cavity-solitons of different durations or cavity-solitons with Turing patterns⁷², is generally difficult to generate, as they require a special type of multistability. Hence, such states have only been recently predicted and observed in externally driven systems^{73,74}.

Microcombs based on a nested cavity configuration are naturally multimodal systems, so the coexistence of states having different natures for a fixed cavity setting occurs more readily. In principle, these states are free to appear anywhere within the microcavity linewidth. As we have recently shown⁴³, however, the slow nonlinearities effectively govern the system's dominant state, selected by choosing appropriate values for a reduced set of global parameters. The observation of such a soliton-CW bonded state in very different settings, with microcavities of different natures⁷¹, indicates that these states are common and naturally robust. Counterintuitively, the interactions between solitons and a CW can provide a strong long-term stability^{71,75}. The reason for their formation in microresonator-filtered lasers, however, is not yet clearly understood.

Here, we study the nonlinear formation and recovery of a bonded state comprising a soliton and a CW, respectively red and blue locked on the microcavity resonance slopes. We reveal that the blue-detuned continuous wave and soliton form in two distinct regions of the erbium laser spectrum, where the slow resonant nonlinearity of the amplifier has a different sign. The physics of this state is particularly rich, and our real-time measurements, implemented via DFT, show that the slow and fast dynamics are deeply interconnected and mediated by the modal structure of the system. Our key observation is the formation of a nonlocal bonding of these composite states. These interactions reveal the main physics sustaining the system dominant attractors, and here we show how to use the gain refractive index dispersion to induce such a state.

Results and discussion

Our system consists of a focusing Kerr microcavity based on an integrated micro-resonator in anomalous dispersion regime coupled to an Er-doped fibre amplifying cavity (Fig. 1a and Fig. S1) and including a free-space delay line to match the group delay of the cavities and an intracavity bandpass filter to select the gain bandwidth (Methods). Our intracavity passband filter is very broad and does not induce phase-related effects. In our current implementation, the free spectral range (FSR) of the microcavity is ~ 48.89 GHz and the linewidth of the microcavity resonances is ≈ 120 MHz. The FSR of the main cavity (FSR_B) is < 100 MHz (~ 92 MHz), allowing in principle multiple resonances of the main cavity to lase within the same microcavity resonance and multi-modal operation to take place. CWs and Turing patterns usually appear on the blue-detuned slope of the microcavity, where microcavities with a focusing Kerr nonlinearity display monostable behaviour, while solitons appear on the red-detuned slope of the microcavity, where the system is bistable^{43,76}. The slow nonlinearities of the two cavities (i.e., thermal detuning and gain saturation) affect the resonance positions which shift as a function of the optical energy and hence the working regime of the laser. In our system, both the microcavity and the erbium fibre laser are characterised by a predominantly focusing slow nonlinearity, which red-shifts the resonances with increasing power. As we discussed in ref. 43, when the red-shift of the microcavity dominates, the system will lock to blue-detuned states, forming CWs or Turing pattern. This balance, however, is generally affected by the system loss

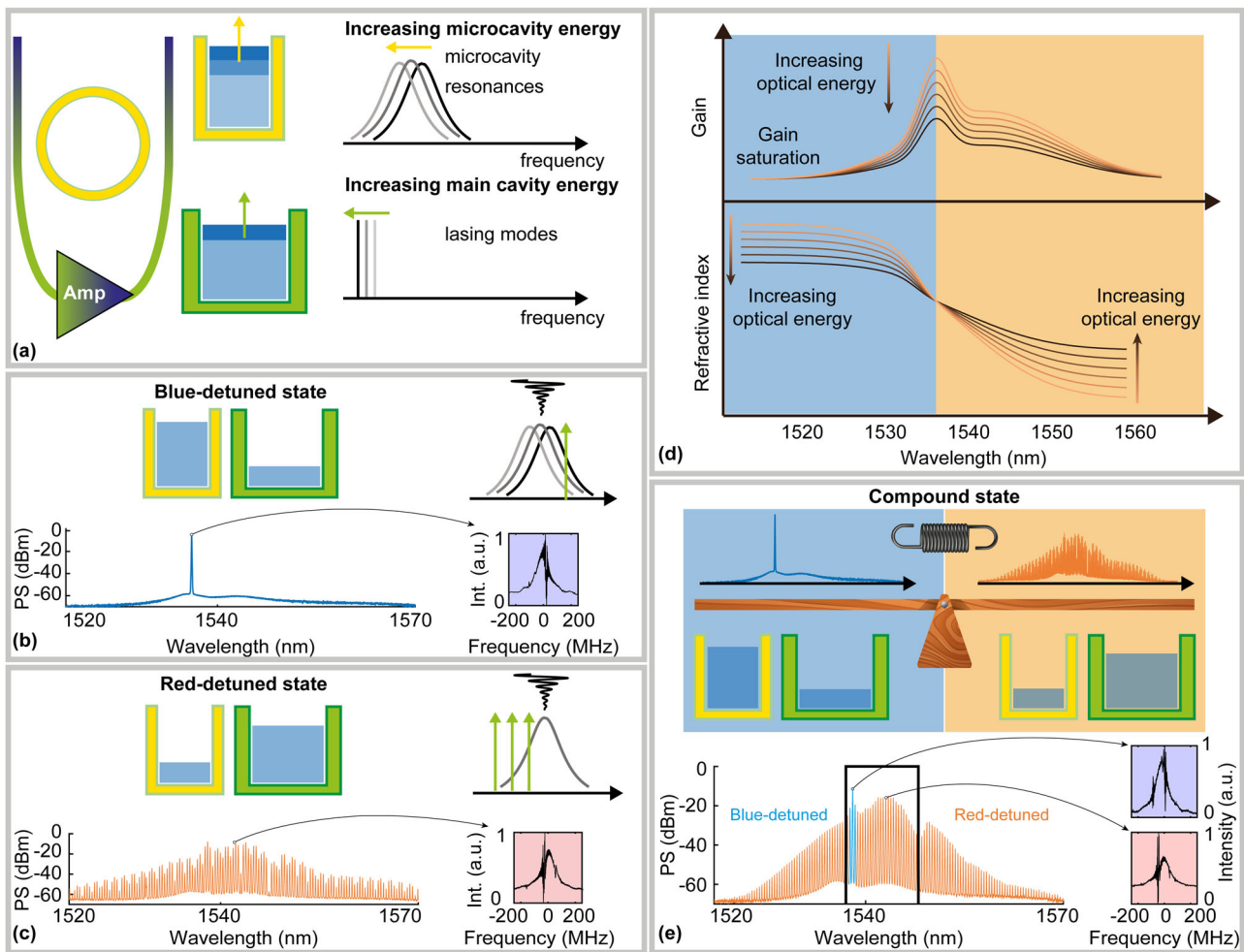


Fig. 1 Coexistence of blue- and red-detuned states. **a** Conceptual diagram of the locking as a result of the energy balance between the main cavity and the microcavity. When the energy increases in the microresonator, its resonances are red-shifted. A similar behaviour can also be found for the main cavity resonances, with an increasing energy producing a red-shift. Depending on the proportion of these two effects, the lasing modes can be blue-detuned or red-detuned with respect to the microcavity resonances. The yellow (green) tank represents the microresonator (main cavity), while the tank level represents the energy level. **b** Example of blue-detuned locking in a continuous wave (CW) state, with the optical spectrum in blue (left) and the laser scanning spectroscopy (LSS) in black (right). **c** Example of red-detuning locking in a two-soliton state, with the optical spectrum in red (left) and the LSS in black (right). **d** Representation of the gain and refractive index spectrum for the erbium-based amplifier, saturating with optical energy. The arrows indicate the sign of the variation following an optical energy increase. **e** State formed by a coexisting, blue-detuned CW and a red detuned soliton, highlighted by LSSs performed in different portions of the spectrum. Note the blue-detuned modes position coinciding with the gain peak position as well as the refractive index step in **(d)** and the red detuned modes being elsewhere. The bandpass filter position is highlighted by the black rectangle superimposed on the optical spectrum of the bonded state in **(e)**.

and gain pump power, and can be tuned to have a predominantly red shift in the laser modes, to obtain soliton states. In Fig. 1b, c, we show an example of a blue-detuned CW state and a red-detuned two-soliton state respectively, whose locking detuning can be inferred from laser scanning spectroscopy measurements (LSS), here shown at different microcavity modes (see Methods for details regarding the LSS technique).

Interestingly, these two opposite locking behaviours can simultaneously coexist if certain conditions are satisfied. As we can see in Fig. 1d, because of the resonant nature of the gain medium, the refractive index exhibits a step-like response which is related to the specific gain profile by the Kramers–Kronig relationship^{49,77}. The jump in the refractive index, therefore, roughly increases with the increasing resonant gain. We notice that this gain is also affected by the amplified light in the fibre that, when it increases, causes the gain to saturate. This reduces the amplitude of the refractive index step and produces a refractive index variation of opposite sign before and after

the step position. Longer wavelengths will then experience an increase in refractive index, whilst shorter wavelengths will experience a decrease. Although the slow nonlinearity of the erbium laser, which is dominated by thermal effects, is self-focusing in both cases, such a step can change the balance between the thermal nonlinearity of the microcavity and favour either blue or red-detuned states in different spectral regions. For the case studied here (Fig. 1e), a red-detuned single soliton state coexists with a few blue-detuned lines, whose emergence is favoured by the peak in the gain profile of the Er-doped fibre amplifier. Experimentally, we use an intracavity filter to select a portion of the erbium gain around the refractive index step in order to observe both behaviours at the same time (Fig. 1e). This creates a coexisting CW and soliton state in the two different spectral regions. A LSS measurement of the resonance shows red-detuned lines in the spectral region where the soliton is dominant, and a coexistence of red and blue-detuned states where the CW lines are present, indicating that these states are superimposed on

the soliton state. We will show that the two locking mechanisms act together to stabilise the whole microcomb.

Model. We start with the model utilised in our previous literature^{42,43,76,78}. We consider that the normalised slowly varying amplitudes of the electric fields are $a(x, t)$ in the microcavity and a superposition of $2N + 1$ super-modes $b_q(x, t)$, being q the mode order, in the amplifying loop. In all our simulations, we use $N = 7$, i.e., we account for 15 main cavity modes per microcavity resonance. The time t is normalised with respect to the roundtrip time of the amplifying loop, while the space x is normalised with respect to the microcavity length. The field $a(x, t)$ is defined for $0 < x < 1$, and we use the same definition for the amplifying field, based on the super-mode expansion. The equation for the amplifying cavity modes is expressed in the Fourier domain with f_x spatial frequency and $\tilde{b}_q(f_x) = \int b_q(x) \exp(2\pi i f_x x) dx$. With these definitions, the system reads

$$\partial_t a = \frac{i\zeta_a}{2} \partial_{xx} a + 2\pi i \Delta_a a + i|a|^2 a - \kappa a + \sqrt{\kappa} \sum_{q=-N}^N b_q, \quad (1)$$

$$\begin{aligned} \partial_t \tilde{b}_q = 4\pi^2 \left(-\frac{i\zeta_b}{2} + \sigma \right) f_x^2 \tilde{b}_q + 2\pi i (\Delta_b - q) \tilde{b}_q \\ + g(f_x) \tilde{b}_q - \sum_{p=-N}^N \tilde{b}_p + \sqrt{\kappa} \tilde{a}. \end{aligned} \quad (2)$$

Here the two cavities are group velocity matched and have normalised second order dispersions $\zeta_{(a,b)}$. We also use a gaussian filter with dispersion σ to model the filter which we use to shape the gain bandwidth. The two equations are dissipatively coupled by the constant κ , representing the normalised roundtrip loss of the microcavity. The gain parameter is g and the cavity-frequency offsets are $\Delta_{(a,b)}$ in units of the amplifying cavity FSR, which depend on the energies $E_a = \int_0^1 |a|^2 dx$, $E_b = \sum_{q=-N}^N \int_0^1 |b_q|^2 dx$. Specifically, we set $\Delta_a = \Delta_{Ta}$, with Δ_{Ta} obeying to the following equation:

$$\tau_{Ta} \partial_t \Delta_{Ta} = -\Delta_{Ta} + \Gamma_{Ta} E_a(t). \quad (3)$$

This equation models the thermal behaviour. As done previously⁴³, we approximate the thermal response with a single equation for the microcavity, with Γ_a being a nonlinear coefficient designed to compensate for the effects of the amplifier and τ_{Ta} being the timescale, here normalised against the fibre cavity roundtrip T_b . The detuning in the amplifying cavity equation is ruled by the properties of the gain material, so it is helpful to define first the gain equation.

In particular, for the fibre amplifier, by standard Maxwell-Bloch formalism with the approximation of a fast decay of the potential², the saturable gain g_0 is

$$\partial_t g_0 = -\frac{g_0}{\tau_g} (1 + \eta E_b(t)) + \frac{g_p}{\tau_g}, \quad (4)$$

where η is a normalised inverse of the saturation energy, τ_g the gain decay time constant and g_p the pumping gain. Here g_0 is a real variable. Our erbium amplifier is characterised by a narrow peak at 1536 nm and a broad peak extending at longer wavelengths which we consider flat, as we use a bandpass filter σ (~ 12 nm) to limit the working region. We express the gain as

$$g(f_x) = g_0 \left(1 + \gamma \exp\left(-\frac{(f - f_0)^2}{f_w^2}\right) \right), \quad (5)$$

with f_0 and f_w frequency centre and width of the gain resonance. The variable γ represents the amplitude of the resonance (the excess of gain compared to the central reference wavelength).

The amplifier refractive index change due to the gain saturation is generally frequency dependent and results from the Kramers—Kronig integral of the difference between the absorption and the gain spectra. In general, the relationship yields a decrease in the refractive index on the blue side of the spectrum and increase of the refractive index on the red side of the spectrum, depicted in Fig. 1d. The detuning for the amplifying cavity can be then defined as $\Delta_b = \Delta + \Omega(f_x)$, with Δ a fixed relative detuning, and $\Omega(f_x)$ a frequency and gain dependent term taking into account Kramers—Kronig relations. Here we use a simplified function and consider only a step detuning, which changes sign around the gain resonance at f_0 :

$$\Omega(f_x) = g_0 \Omega_0 \text{sign}(f_x - f_0). \quad (6)$$

The parameter Ω_0 models the strength of the change and is positive for a focusing nonlinearity. The system effectively sees two different types of nonlinearities between the resonance points, as it is well established in the literature on laser amplification^{49,77}. The parameter f_0 allows one to move the position of the filter with respect to the erbium laser gain resonance. For large positive values of f_0 , this modelling results in pure soliton formation (Fig. S2), as $\Omega(f_x) < 0$ for most of the microcavity resonances. However, with $f_0 = 10$, i.e., ten microcavity modes away from the centre, we can promote the formation of a CW state at the peak of the gain with a soliton state and hence, demonstrate coexisting behaviour. For larger positive values of f_0 , the soliton state is favoured compared to the CW, because $\Omega(f_x) < 0$ for most of the microcavity resonances. This modelling results in pure soliton formation for larger values (Fig. S2 reports an example for $f_0 = 20$), which is consistent with our experimental findings.

Figure 2a–d reports the microresonator spatial and spectral intensity evolution during the formation of the bonded state and resulting outputs for $f_0 = 10$ (see Methods for the parameters). The output intensity profiles of the microresonator (Fig. 2b, green) suggest a modulated pulse, carrying the clear signature of a soliton (pulse) with a CW element (modulation), which is apparent in the spectral profile (Fig. 2d, green). Compared with the gain profile (Fig. 2d, yellow), the CW mode is aligned to the peak gain and refractive index step (black line), while the soliton carrier mode is centred to the gain in the region of low refractive index. In Fig. 2e, we plot the evolution of the relative detuning $\Delta + \Omega(f_x) - \Delta_{Ta}$ at different frequencies. For $f_x < f_0$ (e.g., soliton carrier) the detuning increases (red-detuned locking), while for frequencies close to the CW mode, the detuning decreases (blue-detuned locking). Such an effective dispersion on the detuning causes the soliton and the CW mode to exhibit distinct carrier frequency offsets, depicted in Fig. 2f as red and blue respectively. Specifically, the soliton operates at a frequency of 0.8 FSR, whereas the CW mode is 0.2 FSR, showing a blue deviation from the soliton value. The simulated radio frequency (RF) output at $x = 0$ (Fig. 2f), hence, shows a predominant DC component related to the average pulse power and a beat-note at $\approx 0.6 \text{FSR}_B$ resulting from the beating between the soliton and CW frequency offsets. The coexistence is also noticeable in the energy distribution of the super-modes: the main super-mode (Fig. 2b, d in red) supports the soliton pulse while the higher order blue-detuned (in blue) super-mode is filled with a quasi-CW state. The dynamic process to get to this state shows a first set of high energy, Q-switched bursts until reaching modulational instability and solitary propagation (Fig. 2g), accompanied by energy exchanges between the microcomb modes and a progressive saturation of the gain. The final solitary state (Fig. 2h) clearly show the interference with the CW state. We will discuss this further in the context of our experimental results.

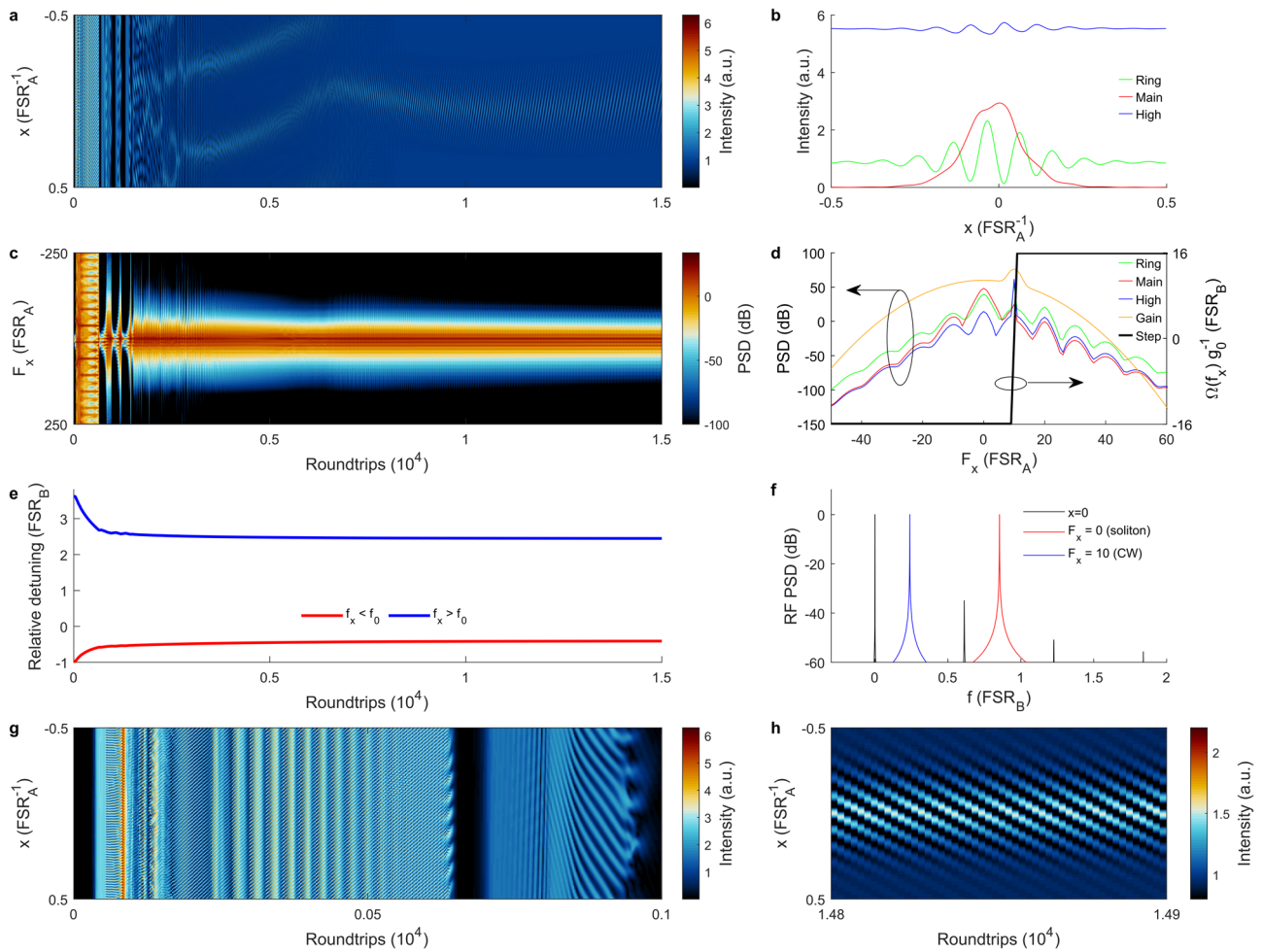


Fig. 2 Simulation of a bonded state starting-up from noise. a Microresonator intensity in the direct space (x) versus simulation time. **b** Intensity profiles of the microresonator (green), main supermode (red) and higher order supermode (blue) at the last temporal slice. **c** Power spectral density in the reciprocal space (F_x) of the field in (a). **d** Power spectral density profiles of the microresonator (green), main supermode (red) and higher order supermode (blue) at the last temporal slice along with gain (yellow) and refractive index (black) profiles. **e** Detuning plot of the quantity $\Delta + \Omega(f_x) - \Delta_{TA}$ at frequencies below and above the refractive index step at f_0 versus simulation time. **f** Radio frequency spectrum, calculated from $t > 14,000$ for the microcavity field at a fixed point $x = 0$ (black), with temporal spectrum of the $f_x = 0$ component (red) and $f_x = 10$ component (blue) of the microcavity field. **g** Zoom at the beginning of (a). **h** Zoom at the end of (a) showing stable solitary propagation with modulations in the form of diagonal stripes. Simulation data obtained integrating Eqs. (1-6) with parameters in the Methods.

Start-up of the bonded state. In Fig. 3a, we used the DFT technique (see Methods and Fig. S3 for its calibration against optical spectra) to capture the fast spectral dynamics arising during formation of the single soliton state with coexisting CW state. Specifically, we stretch the pulse with a ~ 10 km long high dispersion fibre ($D = -1360$ ps/nm), in order to observe the spectral features of the state in the temporal domain. As we operated in a regime of high repetition rate (48.89 GHz) and large bandwidth (>60 nm), which is generally difficult to handle in DFT due to pulse overlapping, the soliton train is gated through amplitude modulation with a 300 ps window signal at ~ 33 MHz (see Fig. S4 for a simulation of a gated DFT for a pulse train derived from the state in Fig. 2). Hence, our real time traces show the spectrum of a bundle of about 10 consecutive pulses at a 33 MHz repetition rate, which is more than sufficient to study the slow dynamics of our system (~ 0.1 ms). The use of gating also improves the DFT technique under the presence of the CW state, which gets pulse-shaped and would otherwise cause detrimental interference effects. A DFT measurement generally brings the information of the RF noise of the pulses superimposed on the traces. While this is usually disregarded, this information is very

useful in our case as the RF noise carries the information of the frequency beating of the modes where soliton and CW lines coexist (Fig. S5). We use the combination of these two effects to study, in real time, both the fine frequency and optical evolution of the system.

We started the system in a CW regime (see Fig. 3b, top and 3c). The CW state is formed at $\lambda \approx 1543.2$ nm, which is in the low refractive index region of the erbium amplifier, where solitons are observed. After a quick (milliseconds) adjustment of the filter towards the short wavelengths, the system showed a Q-switched behaviour, with energy exchange between the microcomb modes, until it reached a bonded state (Fig. 3b, bottom and 3d) with a soliton centred around $\lambda \approx 1543.5$ nm and a CW state centred at $\lambda \approx 1536.7$ nm. As soon as the bonded state emerges, a clear beating effect appears in the DFT trace (see Fig. S5 for a detailed explanation on this aspect).

It is instructive to compare the experimental results with theory (see Fig. 4). In Fig. 4a–d, we focused our attention on two specific start-up dynamics. The first (Fig. 4a, b) is the energy exchange between the strongest microcavity modes of the state, namely the soliton carrier ($F = 0$, $\lambda \approx 1543.5$ nm) and one of the

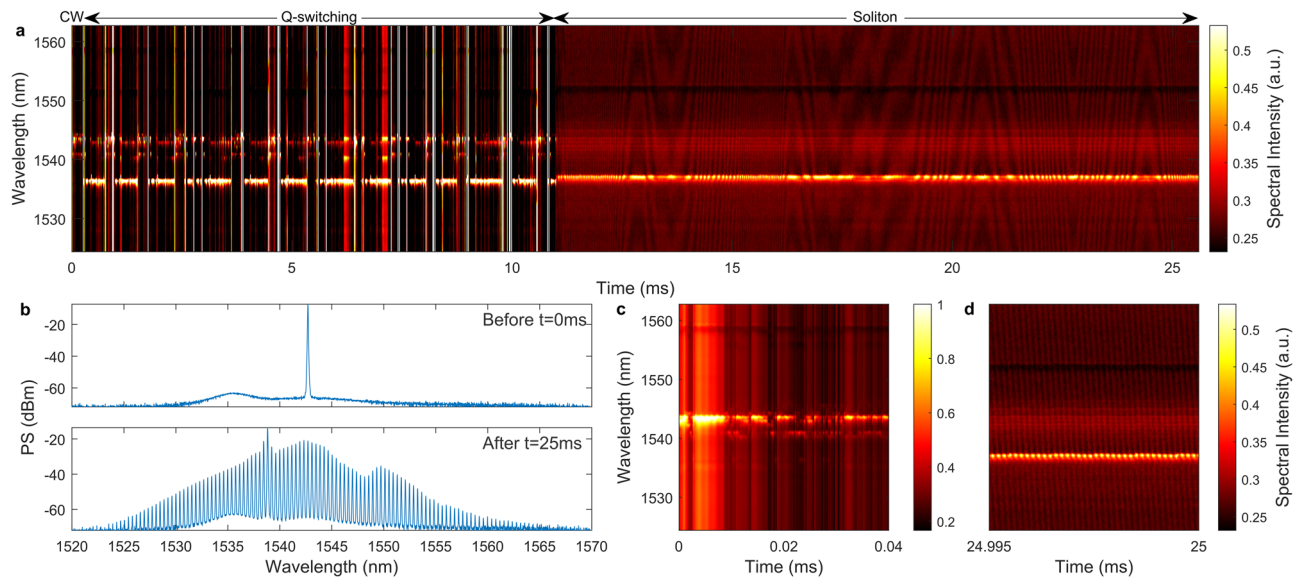


Fig. 3 Start-up of the bonded state after adjustment of the intracavity filter. **a** Dispersive Fourier Transform (DFT) trace showing transition between a continuous wave (CW) state and the single soliton with coexistence. **b** Optical spectrum of the CW state before the DFT acquisition (top) and after the DFT acquisition (bottom) taken with an optical spectrum analyser. **c** Zoom of the DFT trace at the beginning of (a) indicating the start of the transition. **d** Zoom at the end of (a) showing stable solitary operation with a periodical modulation due to the coexistence between the soliton and the blue-detuned CW state.

blue-detuned coexisting modes ($F = 10$, $\lambda \approx 1536$ nm). During this initial phase, the system is not able to support the simultaneous existence of these modes, since they compete with each other. One way to explain this oscillatory behaviour is by considering the role of the slow nonlocal nonlinearities; the system may briefly support a state, but its energy will determine a change of the global parameters which may cause the state to break after some time; new states would then cyclically emerge until the system finds a viable state whose microcavity and main cavity energy balance produces a suitable detuning. In other words, the nonlocal nonlinearities constrain the optical energy of the states and, under specific conditions, enhance their robustness by implementing in turn an energy-detuning feedback⁴³. In the experimental configuration of this study, the system satisfied its energetic balance when the bonded state appeared. During the formation stage, both experiments and theory highlight a recurring exchange of energy between the spectral region of the soliton and blue-detuned CW state. As can be seen in Fig. 4c, d, the two sub-states started coexisting with multiple breaks until the system developed into stable operation. When this happened, the modes of the comb became extremely narrow, and the RF noise showed clear beat-notes both theoretically (Fig. 4e) and experimentally (Fig. 4f and Fig. S5c). We have extracted the frequency of this beat-note in our simulations (Fig. 4g) and for the experiment (Fig. 4h) immediately after soliton formation. In both cases, the system showed a first order relaxation dynamic, indicating that the system still evolved for some time after the appearance of the state, likely driven by the intrinsic nonlocal feedback which experimentally settled in less than 200 μ s⁴³.

Bonded state self-healing. As a final case-study, we focused on the fast recovery mechanisms which enhance the robustness of the state. We perturbed a stable bonded state by inducing a quick change on the main-cavity length (see Methods) of ~ 2 μ m and we studied how the system reacted to this abrupt perturbation (Fig. 5). The soliton state was lost for < 5 ms (Fig. 5a). Specifically, the state in Fig. 5b (top) initially breaks into an unstable comb

(Fig. 5c), which leads to the CW state multiple times (one of these transitions is shown in Fig. 5d) guiding the recovery eventually happening in Fig. 5e, with the final state plotted in Fig. 5b (bottom). Following the same analysis of Fig. 4h, we retrieved the frequency variations of the coexistence beat-note (Fig. 5f), and we show how the system initially drifts away from its original conditions until the state is lost (start until 4.8 ms). Subsequently, the nonlocal feedback will act as a “return spring” bringing the soliton back in stable conditions after a few damped frequency oscillations (8.9 ms until the end). Note the different frequency which the system settles to at the end of the experiment (0.8% increase with respect to the initial value), indicating the reaction of the feedback mechanism necessary to reach the equilibrium at the new cavity length conditions.

Conclusions

In this study we have shed light on the mechanisms and dynamics involved in the formation of solitons with significant presence of a coexistent CW component. This particular bonded state appears due to the dispersion in the nonlinear refractive index of the erbium fibre. The soliton and continuous wave appear in two discrete spectral regions of the gain and interact elastically. The modal structure mediates their existence, but their equilibrium is maintained by their relative nonlocal potential. Surprisingly, these states see a different effective global nonlinearity due to the gain dispersion and which is mediated by both the microcavity and the fibre slow nonlinearities. Their formation is characterised by fast energy exchange between their respective spectral regions until an energetically viable composite is formed, which shows damped oscillations, a signature of elastic bonding, until stability is reached. The CW state, moreover, acts as an additional energy reservoir further thermally stabilising the system. Our experiments show that this state is robust and appealing for out-of-the-lab applications. Our theoretical modelling explains the origin of the state, linked to the step-like response of the nonlinear refractive index of the amplifier. Such a bonded state is well suited for studying the real-time evolution of the system, as the behaviour of the nonlocal feedback is visible in the energy exchange

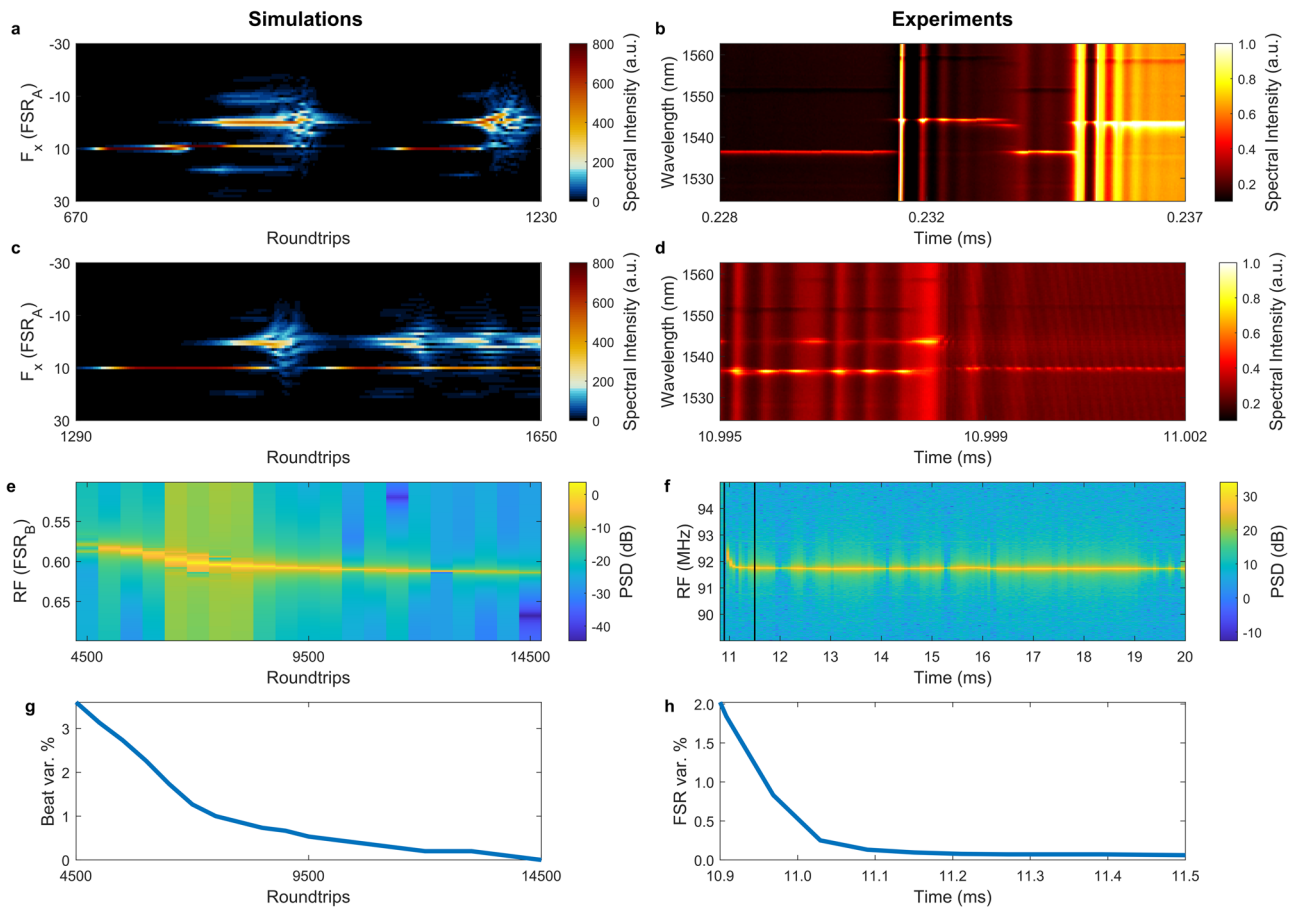


Fig. 4 Formation dynamics. **a** Zoom of the temporal evolution of the spectrum in the simulation of Fig. 2 showing the energy exchange between the blue-detuned mode and the soliton carrier comb line. The dynamic repeats in a Q-switching behaviour. **b** Zoom of the Dispersive Fourier Transform (DFT) trace in Fig. 3a, showing the same energy exchange between the comb modes and the Q-switching dynamic in qualitative agreement with **(a)**. **c** Zoom of the temporal evolution of the spectrum in the simulation of Fig. 2, showing the final energy exchange before soliton formation. **d** Zoom of the DFT trace in Fig. 3a, in qualitative agreement with **(c)**. **e** Radio frequency (RF) spectrum evolution for the microcavity field (at a fixed point $x = 0$) obtained from the simulation in Fig. 2. **f** RF spectrum extracted from the DFT trace in Fig. 3. After the bonded state has formed, we can see a clear beat-note around the main cavity free spectral range (FSR) frequency. **g** Relative variation of the beat-note frequency extracted from **(e)**. **h** Coexistence beat-note frequency extracted from the boxed data in **(f)** and plotted against time.

between the different spectral components of the coexisting CW and soliton states during the formation stage. When the bonded state is reached, the coexistence is revealed in the RF noise. Our real-time DFT measurements highlight the role of the nonlocal feedback in the start-up, recovery and stabilisation of solitary states. The presence of coexisting, blue-detuned modes assists in preserving the soliton states, even after significant perturbations are applied.

Although this study focuses on the dynamics behind the formation and recovery of a composite between a soliton and a quasi-CW state, the multi-modal structure of our topology may support a variety of coexistent states. As an example, similarly to the quasi-CW state, Turing patterns could be also able to coexist with laser cavity-solitons as they are blue-detuned, a scenario which could be worth exploring in future works.

Methods

Numerical parameters. In our simulations we used: $N = 7$, $\zeta_a = 1.25 \times 10^{-4}$, $\zeta_b = 3.5 \times 10^{-4}$, $\sigma = 1.5 \times 10^{-4}$, $\kappa = 2\pi$, $\Gamma_{Ta} = 2$, $\tau_{Ta} = 4000$, $\eta = 0.1$, $\tau_G = 8000$, $\gamma = 6$, $f_W = 2$, $\Omega_0 = 15.9$. For the case of Fig. 2, we used: $\Delta = 1.321$, $g_0 = 0.144$, $f_0 = 10$. For the case of Fig. S2, we used: $\Delta = 1.326$, $g_0 = 0.15$, $f_0 = 20$. Note that the microring here does not

include intrinsic losses, discussed instead in ref. 44 concerning conversion efficiency. However, from a qualitative perspective, adding this parameter does not alter significantly the dynamics exhibited by our laser, justifying its absence in the model presented in this manuscript.

In Fig. 2f, we calculated the frequency carrier offset of the soliton and the CW by the Fast Fourier Transform (FFT) of the temporal series of the microcavity field components at $f_x = 0$ and $f_x = 10$, which are respectively related to the soliton and the CW state.

Setup. Our experimental setup consists of a nonlinear microcavity nested in a longer amplifying fibre cavity (Fig. S1). The two main elements that are used to control the pulse formation are an Erbium Doped Fibre Amplifier (EDFA), whose gain bandwidth is limited by a bandpass filter, and an adjustable delay line, used to modify the cavity length, thus the mode spacing. By only adjusting these parameters, we manage to obtain a broad range of regimes, such as the recently described laser cavity-solitons^{42–44}. As this study is focused on the laser cavity-soliton regime, the setup parameters are tuned accordingly. Laser cavity-solitons obtained from this setup present a 60 nm FWHM bandwidth, at a repetition rate of 48.89 GHz.

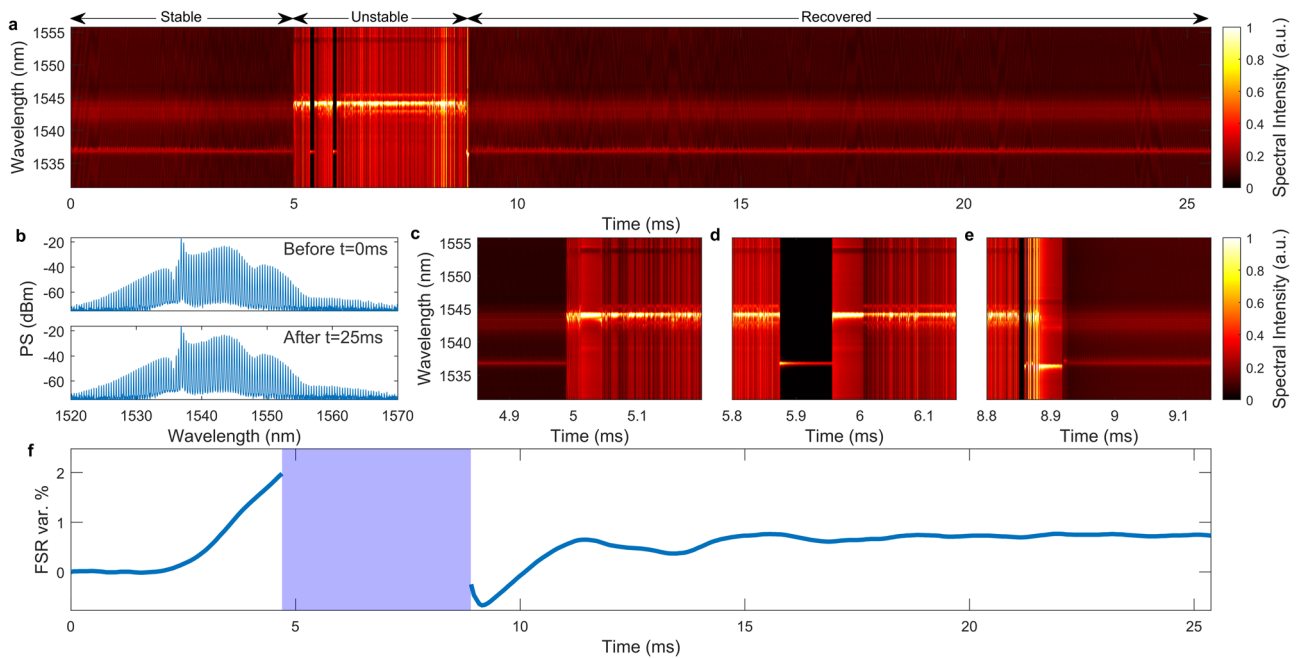


Fig. 5 Soliton self-healing dynamics after an abrupt cavity-length perturbation. **a** Dispersive Fourier Transform (DFT) trace showing the self-healing dynamic. **b** Optical spectrum before (top) and after (bottom) the DFT acquisition. **c** Zoom of **(a)** showing the transition between stable solitary and Q-switching dynamic. **d** Zoom of **(a)** showing transitions between Q-switching regimes and continuous wave regimes at wavelengths of the blue-detuned coexistent modes and soliton carrier. **e** Zoom of **(a)** showing the recovery of the solitary state. **f** Extraction of the coexistence beat-note before and after the state is destroyed, showing damped oscillations during recovery. The blue-region corresponds to the Q-switching dynamics where the radio frequency noise is broad.

Laser scanning spectroscopy (LSS). To retrieve the position of the lasing modes with respect to the hot microcavity resonances, a frequency-swept CW source is injected at the Through port of the microresonator by means of a circulator. Therefore, the CW signal is injected counter-propagating to the normal laser direction to be then extracted at the Add port and photodetected. The recorded signal contains information regarding the profile of the microcavity resonances with a superposition of the beat-notes between the CW source and the back-scattered lasing modes, which allows to retrieve the detuning parameters. For more information, refer to refs. ^{42,43}.

Modulated DFT and few-pulses-approximation. To apply a real time diagnostic to these pulses using DFT, the repetition rate of the pulses must be decreased first. Indeed, applying DFT to ultrashort pulses significantly stretches the pulses, in this case a factor of $\sim 10^6$. This pulse broadening will inevitably lead to pulse overlapping in this case, thus information losses which must be avoided. This problem is solved by optically sampling our laser emission rate at a reduced repetition rate using intensity modulation. By lowering the repetition rate to a value close to 33 MHz, we manage to reduce the signal duty cycle thus allowing pulses temporal stretching without overlap. Nevertheless, as our modulation system speed does not allow for selecting single pulses, bunches of ~ 10 pulses are kept and the approximation that these can be considered as one average pulse is made. We justify this approximation by the fact that this study is focused over longer timescales for which the pulse-to-pulse variation is negligible. Thus a 10-pulse bunch can be considered as one average pulse, allowing us to study the spectral evolution over longer timescales (i.e., >30 ns). Because of this approach, the DFT loses the ability to resolve the spectrum of a single optical pulse, gathering instead information on the spectrum of the bunch of pulses. This leads to a comb-like DFT signal which can be

calibrated against an optical spectrum analyser (OSA) trace (see Fig. S3 for the calibration and Fig. S4 for a simulation of the gated DFT technique).

The gating step is achieved using a 3 GHz pulse generator (Keysight 8133 A) with a 10 Gb/s LiNbO₃ Optical Intensity Modulator. The signal is modulated over a 300 ps width window. The modulated signal can then be submitted to the DFT diagnostic, converting the spectral profile of the pulses into a temporal profile. To do so, a 10 km-long Telecom Dispersion-Compensating Fibre (DCF) is used, with a dispersion of $D = -1360$ ps/nm ($\beta_2 = 1730$ ps² at 1550 nm). Using this technique, one must be careful about the peak power of the input pulses, as nonlinearities can be easily exhibited by femtosecond pulses in dispersive fibres. DFT is not supposed to influence the spectral profile of the pulse, thus the quality of the pulses and the effect of nonlinearities is checked by comparing the spectra before and after travelling through the DCF. The effective dispersion needed for this setup is estimated using the so-called far field condition, which consists of the effective length of fibre needed for the pulse to adopt the temporal shape of its spectrum, here a ~ 10 km long high dispersion fibre ($D = -1360$ ps/nm). The pulse train is finally acquired using a 15 GHz bandwidth photodetector (EOT 3500-F) connected to a fast oscilloscope (Lecroy LabMaster MCM-Zi @ 10 Gsa/s, 4 GHz bandwidth), yielding an equivalent DFT spectral resolution below 200 pm. The pulse generator and oscilloscope's time base clocks are derived from the same source to ensure synchronism and eliminate temporal drifts. A simple algorithm is then used to process the data and display it in a 2D graph, by stacking the DFT spectra over time.

An important feature of the DFT technique is that it allows to measure at the same time the RF beating and the optical spectrum. This is particularly useful for our set of states, because the RF spectrum shows the real-time frequency detuning between

the soliton state and any other additional mode coexisting with it. A typical example of this type of measurement is in Figs. 3–5, where the DFT traces show, along with the optical spectrum, a strong transversal modulation related to the frequency difference of the red- and blue-detuned modes within a microcavity resonance. We explain this phenomenon with Fig. S5, where we have considered a couple of blue- and red-detuned modes in a microcavity resonance at a frequency difference $F_0 = 92$ MHz, and their sidebands obtained after intensity modulation takes place (Fig. 4a). In Fig. 4b, we estimated the radio frequency spectrum of the photocurrent associated to the frequency components in Fig. 4a. Note the presence of sidebands around each harmonic of the modulating frequency $f_m = 32.7$ MHz. The difference Δf between the harmonics and their respective sidebands is found to be $\Delta f = |F_0 - Nf_m|$, where N is the integer which gives the smallest Δf . In the case considered, $N = 3$ and $\Delta f \approx 6$ MHz. This modulation at Δf is related to the transversal modulations visible in the DFT traces.

Data availability

The data that support the plots within this manuscript have been deposited on Loughborough University Research Repository⁷⁹. All other data used in this study are available from the corresponding authors upon reasonable request.

Received: 31 March 2023; Accepted: 4 September 2023;

Published online: 20 September 2023

References

- Nicolis, G. & Prigogine, I. *Self-Organization in Nonequilibrium Systems: from Dissipative Structures to Order through Fluctuations* (Wiley-Blackwell, 1977).
- Lugiato, L. A., Prati, F. & Brambilla, M. *Nonlinear Optical Systems* (Cambridge University Press, 2015).
- Grelu, P. & Akhmediev, N. Dissipative solitons for mode-locked lasers. *Nat. Photonics* **6**, 84–92 (2012).
- Davydov, A. S. *Solitons in Molecular Systems* vol. 4 (Springer Netherlands, 1985).
- Yakushevich, L. V. *Nonlinear Physics of DNA*. (Wiley-VCH, 2004).
- Kippenberg, T. J., Holzwarth, R. & Diddams, S. A. Microresonator-based optical frequency combs. *Science* **332**, 555–559 (2011).
- Pasquazi, A. et al. Micro-combs: a novel generation of optical sources. *Phys. Rep.* **729**, 1–81 (2018).
- Marin-Palomo, P. et al. Microresonator-based solitons for massively parallel coherent optical communications. *Nature* **546**, 274–279 (2017).
- Xu, X. et al. 11 TOPS photonic convolutional accelerator for optical neural networks. *Nature* **589**, 44–51 (2021).
- Suh, M.-G. & Vahala, K. J. Soliton microcomb range measurement. *Science* **359**, 884–887 (2018).
- Brasch, V. et al. Photonic chip-based optical frequency comb using soliton Cherenkov radiation. *Science* **351**, 357–360 (2016).
- Spencer, D. T. et al. An optical-frequency synthesizer using integrated photonics. *Nature* **557**, 81–85 (2018).
- Huang, S.-W. et al. A broadband chip-scale optical frequency synthesizer at 2.7×10^{-16} relative uncertainty. *Sci. Adv.* **2**, e1501489 (2016).
- Hu, H. et al. Single-source chip-based frequency comb enabling extreme parallel data transmission. *Nat. Photonics* **12**, 469–473 (2018).
- Feldmann, J. et al. Parallel convolutional processing using an integrated photonic tensor core. *Nature* **589**, 52–58 (2021).
- Riemensberger, J. et al. Massively parallel coherent laser ranging using a soliton microcomb. *Nature* **581**, 164–170 (2020).
- Liu, J. et al. Monolithic piezoelectric control of soliton microcombs. *Nature* **583**, 385–390 (2020).
- Corcoran, B. et al. Ultra-dense optical data transmission over standard fibre with a single chip source. *Nat. Commun.* **11**, 2568 (2020).
- Pfeifle, J. et al. Optimally coherent Kerr combs generated with crystalline whispering gallery mode resonators for ultrahigh capacity fiber communications. *Phys. Rev. Lett.* **114**, 093902 (2015).
- Kues, M. et al. On-chip generation of high-dimensional entangled quantum states and their coherent control. *Nature* **546**, 622–626 (2017).
- Prati, F. et al. Soliton dynamics of ring quantum cascade lasers with injected signal. *Nanophotonics* **10**, 195–207 (2020).
- Meng, B. et al. Mid-infrared frequency comb from a ring quantum cascade laser. *Optica* **7**, 162–167 (2020).
- Shen, X., Choi, H., Chen, D., Zhao, W. & Armani, A. M. Raman laser from an optical resonator with a grafted single-molecule monolayer. *Nat. Photonics* **14**, 95–101 (2020).
- Meng, B. et al. Dissipative Kerr solitons in semiconductor ring lasers. *Nat. Photonics* **16**, 142–147 (2022).
- Piccardo, M. et al. Frequency combs induced by phase turbulence. *Nature* **582**, 360–364 (2020).
- Dutt, A. et al. On-chip dual-comb source for spectroscopy. *Sci. Adv.* **4**, e1701858 (2018).
- Liang, W. et al. High spectral purity Kerr frequency comb radio frequency photonic oscillator. *Nat. Commun.* **6**, 7957 (2015).
- Lei, F. et al. Optical linewidth of soliton microcombs. *Nat. Commun.* **13**, 3161 (2022).
- Jin, W. et al. Hertz-linewidth semiconductor lasers using CMOS-ready ultra-high-Q microresonators. *Nat. Photonics* **15**, 346–353 (2021).
- Volyanskiy, K. et al. Compact optoelectronic microwave oscillators using ultra-high Q whispering gallery mode disk-resonators and phase modulation. *Opt. Express* **18**, 22358–22363 (2010).
- Savchenkov, A. A. et al. Stabilization of a Kerr frequency comb oscillator. *Opt. Lett.* **38**, 2636–2639 (2013).
- Papp, S. B. et al. Microresonator frequency comb optical clock. *Optica* **1**, 10–14 (2014).
- Del’Haye, P. et al. Phase-coherent microwave-to-optical link with a self-referenced microcomb. *Nat. Photonics* **10**, 516–520 (2016).
- Brasch, V., Lucas, E., Jost, J. D., Geiselmann, M. & Kippenberg, T. J. Self-referenced photonic chip soliton Kerr frequency comb. *Light Sci. Appl.* **6**, e16202–e16202 (2017).
- Stern, L. et al. Direct Kerr frequency comb atomic spectroscopy and stabilization. *Sci. Adv.* **6**, eaax6230 (2020).
- Li, B. et al. Reaching fiber-laser coherence in integrated photonics. *Opt. Lett.* **46**, 5201 (2021).
- Leo, F. et al. Temporal cavity solitons in one-dimensional Kerr media as bits in an all-optical buffer. *Nat. Photonics* **4**, 471–476 (2010).
- Barland, S. et al. Temporal localized structures in optical resonators. *Adv. Phys. X* **2**, 496–517 (2017).
- Xu, G. et al. Spontaneous symmetry breaking of dissipative optical solitons in a two-component Kerr resonator. *Nat. Commun.* **12**, 4023 (2021).
- Leonhardt, M. et al. Parametrically-driven temporal cavity solitons in a bichromatically-driven pure Kerr resonator. Preprint at <http://arxiv.org/abs/2206.09533> (2022).
- Engleburt, N. et al. Parametrically driven Kerr cavity solitons. *Nat. Photonics* **15**, 857–861 (2021).
- Bao, H. et al. Laser cavity-soliton microcombs. *Nat. Photonics* **13**, 384 (2019).
- Rowley, M. et al. Self-emergence of robust solitons in a microcavity. *Nature* **608**, 303–309 (2022).
- Cutrona, A. et al. High parametric efficiency in laser cavity-soliton microcombs. *Opt. Express* **30**, 39816–39825 (2022).
- Diallo, S., Lin, G. & Chembo, Y. K. Giant thermo-optical relaxation oscillations in millimeter-size whispering gallery mode disk resonators. *Opt. Lett.* **40**, 3834–3837 (2015).
- Deng, Y., Liu, F., Leseman, Z. C. & Hossein-Zadeh, M. Thermo-optomechanical oscillator for sensing applications. *Opt. Lett.* **21**, 4653–4664 (2013).
- Carmon, T., Yang, L. & Vahala, K. J. Dynamical thermal behavior and thermal selfstability of microcavities. *Opt. Express* **12**, 4742–4750 (2004).
- Rowley, M. et al. Thermo-optical pulsing in a microresonator filtered fiber-laser: a route towards all-optical control and synchronization. *Opt. Express* **27**, 19242–19253 (2019).
- Barmenkov, Yu. O., Kir’yanov, A. V. & Andrés, M. V. Resonant and thermal changes of refractive index in a heavily doped erbium fiber pumped at wavelength 980 nm. *Appl. Phys. Lett.* **85**, 2466–2468 (2004).
- Cutrona, A. et al. Stability of laser cavity-solitons for metrological applications. *Appl. Phys. Lett.* **122**, 121104 (2023).
- He, Y. et al. Self-starting bi-chromatic LiNbO₃ soliton microcomb. *Optica* **6**, 1138–1144 (2019).
- Huang, Y. et al. Temporal soliton and optical frequency comb generation in a Brillouin laser cavity. *Optica* **6**, 1491–1497 (2019).
- Bai, Y. et al. Brillouin-Kerr Soliton Frequency Combs in an Optical Microresonator. *Phys. Rev. Lett.* **126**, 063901 (2021).
- Shu, H. et al. Sub-milliwatt, widely-tunable coherent microcomb generation with feedback-free operation. *Adv. Photonics* **5**, 036007 (2023).
- Shu, H. et al. Microcomb-driven silicon photonic systems. *Nature* **605**, 457–463 (2022).

56. Conti, C., Peccianti, M. & Assanto, G. Route to nonlocality and observation of accessible solitons. *Phys. Rev. Lett.* **91**, 073901 (2003).
57. Chen, Z., Segev, M. & Christodoulides, D. N. Optical spatial solitons: historical overview and recent advances. *Rep. Prog. Phys.* **75**, 086401 (2012).
58. Wang, Z., Nithyanandan, K., Coillet, A., Tchofo-Dinda, P. & Grelu, P. Buildup of incoherent dissipative solitons in ultrafast fiber lasers. *Phys. Rev. Res.* **2**, 013101 (2020).
59. He, R. et al. Analysis of loose bunches of soliton molecules in passive mode-locked fibre laser using time-stretching technology. *Laser Phys. Lett.* **17**, 035105 (2020).
60. Xia, R. et al. Experimental observation of shaking soliton molecules in a dispersion-managed fiber laser. *Opt. Lett.* **45**, 1551–1554 (2020).
61. Liang, H. et al. Real-time dynamics of soliton collision in a bound-state soliton fiber laser. *Nanophotonics* **9**, 1921–1929 (2020).
62. Lapre, C. et al. Real-time characterization of spectral instabilities in a mode-locked fibre laser exhibiting soliton-similariton dynamics. *Sci. Rep.* **9**, 13950 (2019).
63. Kurtz, F., Ropers, C. & Herink, G. Resonant excitation and all-optical switching of femtosecond soliton molecules. *Nat. Photonics* **14**, 9–13 (2020).
64. Chernysheva, M., Sugavanam, S. & Turitsyn, S. Real-time observation of the optical Sagnac effect in ultrafast bidirectional fibre lasers. *APL Photonics* **5**, 016104 (2020).
65. Meng, F., Lapre, C., Billet, C., Genty, G. & Dudley, J. M. Instabilities in a dissipative soliton-similariton laser using a scalar iterative map. *Opt. Lett.* **45**, 1232–1235 (2020).
66. Zeng, J. & Sander, M. Y. Real-time transition dynamics between multi-pulsing states in a mode-locked fiber laser. *Opt. Lett.* **45**, 5–8 (2020).
67. Du, Y., Han, M. & Shu, X. Dark solitons in the exploding pulsation of the bright dissipative soliton in ultrafast fiber lasers. *Opt. Lett.* **45**, 666–669 (2020).
68. Wei, Z.-W. et al. Exploding soliton in an anomalous-dispersion fiber laser. *Opt. Lett.* **45**, 531–534 (2020).
69. Lapre, C., Billet, C., Meng, F., Genty, G. & Dudley, J. M. Dispersive Fourier transform characterization of multipulse dissipative soliton complexes in a mode-locked soliton-similariton laser. *OSA Contin.* **3**, 275–285 (2020).
70. Godin, T. et al. Recent advances on time-stretch dispersive Fourier transform and its applications. *Adv. Phys. X* **7**, 2067487 (2022).
71. Nie, M. et al. Dissipative soliton generation and real-time dynamics in microresonator-filtered fiber lasers. *Light Sci. Appl.* **11**, 296 (2022).
72. Hansson, T. & Wabnitz, S. Frequency comb generation beyond the Lugiato-Lefever equation: multi-stability and super cavity solitons. *J. Opt. Soc. Am. B* **32**, 1259–1266 (2015).
73. Anderson, M. et al. Coexistence of multiple nonlinear states in a tristable passive Kerr resonator. *Phys. Rev. X* **7**, 031031 (2017).
74. Nielsen, A. U., Garbin, B., Coen, S., Murdoch, S. G. & Erkintalo, M. Coexistence and interactions between nonlinear states with different polarizations in a monochromatically driven passive Kerr resonator. *Phys. Rev. Lett.* **123**, 013902 (2019).
75. Zhang, S. et al. Sub-milliwatt-level microresonator solitons with extended access range using an auxiliary laser. *Optica* **6**, 206 (2019).
76. Bao, H. et al. Turing patterns in a fiber laser with a nested microresonator: Robust and controllable microcomb generation. *Phys. Rev. Res.* **2**, 023395 (2020).
77. Thirstrup, C., Shi, Y. & Palsdottir, B. Pump-induced refractive index and dispersions in Er³⁺ doped. *fibers J. Light. Technol.* **14**, 732–738 (1996).
78. Cutrona, A. et al. Temporal cavity solitons in a laser-based microcomb: a path to a self-starting pulsed laser without saturable absorption. *Opt. Express* **29**, 6629–6646 (2021).
79. Cutrona, A. et al. Nonlocal bonding of a soliton and a blue-detuned state in a microcomb laser: Dataset for the article. <https://doi.org/10.17028/rd.lboro.23913063> (2023).

Acknowledgements

This study was supported by grants from EPSRC UKRI (EP/S001018/1 and EP/W028344/1), UK Canada Quantum Technology Programme Innovate UK (77087), ERC (851758 TELSCOMBE), DSTL (DSTLX1000142078), Leverhulme Trust (ECF-2020-537 and ECF-2022-710), ERC (TIMING 725046 and STREAMLINE 950618), French Agence Nationale de la Recherche (ANR-20-CE30-0004), NSERC (Strategic, and Discovery Grants Schemes), Canada Research Chair, City University of Hong Kong (9610395), and MESI PSR-SIIRI Initiatives in Quebec. We thank Dr. Reuben Harding for enlightening discussions.

Author contributions

The experiments in this paper have been performed across the pandemic period. The initial idea was developed by A.P., B.W., M.P., and P.H. P.H. and M.R. have carried out a first implementation of the system with a preliminary study. The measurement and the data analysis of this study have been done by A. Cutrona and V.C. D.D., A. Cooper, L.P. and L.O. supported the experimental work and the data analysis. A.P. and A. Cutrona developed the theoretical and numerical work. S.T.C. and B.L. fabricated the micro-cavities. R.M., D.J.M., J.S.T.G., M.P. and A.P. supervised the research. A.P. and A. Cutrona wrote the initial draft, and all authors contributed to the writing.

Competing interests

The authors declare no competing interests.

Additional information

Supplementary information The online version contains supplementary material available at <https://doi.org/10.1038/s42005-023-01372-0>.

Correspondence and requests for materials should be addressed to Alessia Pasquazi.

Peer review information *Communications Physics* thanks the anonymous reviewers for their contribution to the peer review of this work. A peer review file is available.

Reprints and permission information is available at <http://www.nature.com/reprints>

Publisher's note Springer Nature remains neutral with regard to jurisdictional claims in published maps and institutional affiliations.



Open Access This article is licensed under a Creative Commons Attribution 4.0 International License, which permits use, sharing, adaptation, distribution and reproduction in any medium or format, as long as you give appropriate credit to the original author(s) and the source, provide a link to the Creative Commons licence, and indicate if changes were made. The images or other third party material in this article are included in the article's Creative Commons licence, unless indicated otherwise in a credit line to the material. If material is not included in the article's Creative Commons licence and your intended use is not permitted by statutory regulation or exceeds the permitted use, you will need to obtain permission directly from the copyright holder. To view a copy of this licence, visit <http://creativecommons.org/licenses/by/4.0/>.

© The Author(s) 2023